Romanian Reports in Physics **75**, 602 (2023)

HOLOGRAPHIC MICROSCOPY OF CELL COMPARTMENTS TO BUILD REALISTIC MODELS FOR ELECTRIC FIELD SIMULATIONS

A. M. PLEAVA[1], R. D. NEGOITA[1,2,*], M. A. ILISANU[3], M. MIHAILESCU[4,5,**], M. MOREGA[6], V. L. CALIN[7], E. N. SCARLAT[4], I. A. PAUN[4,8]

[1] CAMPUS Research Center, Politehnica University Bucharest, Romania
[2] Doctoral School of Applied Sciences, Politehnica University Bucharest, Romania
[*] Corresponding author, email: *raluca.negoita@upb.ro*
[3] Doctoral School of Computer Sciences, Politehnica University Bucharest, Romania
[4] Holographic Imaging and Processing Laboratory, Politehnica University Bucharest, Romania
[5] Centre for Research in Fundamental Sciences Applied in Engineering, Politehnica University Bucharest, Romania
[**] Corresponding author, email: *mona.mihailescu@upb.ro*
[6] Faculty of Electrical Engineering, Politehnica University Bucharest, Romania
[7] Biophysics and Cellular Biotechnology Department, University of Medicine and Pharmacy Carol Davila, Bucharest, Romania
[8] Center for Advanced Laser Technologies (CETAL), National Institute for Laser, Plasma and Radiation Physics, Magurele, Romania

Received August 30, 2022

Abstract. The reconstructed phase images (PIs) from digital holographic microscopy contain in each pixel values of the phase shift introduced by the sample in optical path, which allow to segment cells in the most important compartments: nucleus and cytoplasm. Based on PIs, we computed optical properties of cells from two sublines with different malignancy levels and propose a three-layers numerical model to analyze the response under the stress of a high frequency continuous wave electric field. The induced transmembrane voltage is compared for different values of dielectric properties assigned to the cell compartments. Considering the nucleus as a distinct domain with specific electrical properties, brings the model closer to realistic cases; the importance of its presence in simulation models was also investigated.

Key words: digital holographic microscopy, murine melanoma cells, phase images, dry mass, electric field, induced transmembrane voltage.

1. INTRODUCTION

Electroporation (EP) is a non-viral method that facilitates molecules exchanges in living cells by increasing the membrane permeability after exposure to bursts of high electric fields. Depending on time exposure and electric field amplitude, electroporation can be either reversible (the membrane recovers enough rapidly,

and the cell remains viable), or irreversible, which leads to necrosis. This might help either the insertion of drugs (electrochemotherapy) [1, 2] or tissue ablation [3]. Other applications include biotechnology [4] particularly DNA delivery (gene therapy) [5, 6], as well as industrial technology for food manufacture [7], or for biomass processing [8]. It is known that the electrical properties of biological materials depend on the type of cell or tissue due to their complex structures and chemical compositions. To expand the use of EP in new applicative areas or to optimize already established EP-based technologies, the strategy of modelling biological structures and predict their behavior when exposed to electric fields, is a fast, economic, and reliable approach to the problem. For a good quality of such *in silico* models, assigning realistic values of electrical properties – permittivity ε and conductivity σ to each component (mimicking a biological structure), is important [9].

Here we propose a preliminary study to evaluate the induced transmembrane voltage (ITV) under electric stress applied on cells, modelled with their realistic shapes and different values assigned to the dielectric properties of their main components (nucleus, cytoplasm and plasma membrane). At this stage, for the sake of simplicity, the applied electric field is a continuous wave of 1 GHz and 1 kV/cm. At this high frequency, the electric field penetrates easily through the plasma membrane reaching internal organelles and the nucleus; the membrane is no longer an insulating shield, as it is at low frequencies. The realistic shapes of cells were obtained from holographic reconstructed images of the B16 melanoma murine cells. We exploited the advantages offered by the DHM images – phase images (PIs): quantitative information on the optical path difference at single pixel level, very fast acquisition (being a non-scanning technique), the cells are studied in their natural environment and they may relate information about the object phase and amplitude (so DHM can be used for both colourful or transparent objects) [10–12].

We developed in-house codes to segment PIs of the investigated cells and to evidence the most important cellular compartments: nucleus and cytoplasm. The study was performed on four experimental categories of cells with respect to the geometrical shape and to their malignancy level which impact on the optical properties of the cells; these data are further used to develop three-layer cell models for electric field simulations.

2. OPTICAL EXPERIMENTS AND IMAGE PROCESSING

B16 melanoma cells are frequently used as murine model for subcutaneous melanoma. Two cell sublines: B16F10 (highly malignant) and B16F1 (less malignant) were used in our investigations. They were grown in high glucose Dulbecco's modified Eagle's medium, supplemented with 10% fetal bovine serum, in a 37°C and 5% CO_2 incubator. 24 h prior to experiments, the cells were seeded at low

density on 2 cm round microscopic slides. We chose cells with elongated (E) and rounded (R) shapes. Four categories of cells were thus separated to be studied in DHM: B16F1-E, B16F10-E, B16F1-R, B16F10-R.

The slides with culture cells were inserted into the experimental setup for DHM in transmission, off axis configuration. The acquired holograms were preprocessed using dedicated commercial software Koala® based on Fresnel transform to reconstruct 3D images of the cells (Fig. 1). These are considered PIs because they hold information in each pixel about the phase shift introduced by the cell when the laser beam crossed it. Phase shift values are proportional with the local refractive index and cell height; in turn, the refractive index values depend on the protein content (type and concentration) [13].

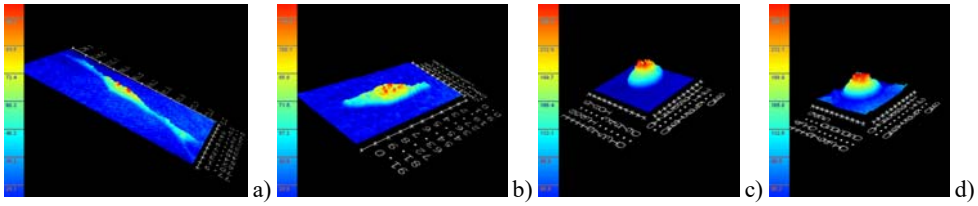

Fig. 1 – 3D representation of PIs for cells categories: a) B16F1-E; b) B16F10-E; c) B16F1-R; d) B16F10-R.

Frequently, the acquired DHM images contained several cells in the optical field of view. Single cell images were obtained by segmentation using a dedicated interface built in Python 3. Before segmentation, three preliminary steps were taken: 1) subtracting the mean and the standard deviation of the phase values aiming to improve the contrast between the region of interest and background, 2) applying a Gaussian filter to blur the image and ensure compact edges of the cells, 3) performing an adaptive binarization based on a threshold computed using Otsu's method. The resulted binary mask was applied on the phase values corresponding to the original image. To maximize the accuracy of the metrics computed for nucleus and cytoplasm, the corresponding masks were adjusted for nucleus, by manual segmentation taking advantage of the relatively good contrast between the cell compartments.

One may see in Fig. 1 representatives of elongated (E) and rounded (R) chosen cells from F1 and F10 sublines. From PI images, we computed mean major axis values for all four cell categories B16F1-E, B16F10-E, B16F1-R, B16F10-R: 62.12 ± 4.35µm, 47.26 ± 3.13 µm, 23.89 ± 1.27 µm, 20.58 ± 1.06 µm respectively. It is obvious that the two classes of cells: elongated and rounded, have sizes with statistically different values and their selection by categories was simple to implement. Phase shifts values were computed separately for cytoplasm (Cyto) and nucleus (Nucl) as mean values across the entire corresponding projected areas (at least 20 PIs were considered for each category).

Table 1

Average values for optical phase shift

	Cyto phase shift (rad)	Nucl phase shift (rad)
B16F1-E	1.04 ± 0.10	1.44 ± 0.11
B16F10-E	1.18 ± 0.11	1.60 ± 0.10
B16F1-R	2.37 ± 0.18	3.50 ± 0.13
B16F10-R	2.68 ± 0.19	4.13 ± 0.14

As Table 1 shows, the highly malignant cells (B16F10) have a higher phase shift than their less malignant counterparts. This difference in phase shifts has been previously explained by different refractive indices of these two categories of malignant cells, in a study combining DHM, cellular proliferation assay and clonogenic tests [14].

3. ELECTRIC FIELD ANALYSIS

Not only the optical properties may vary in relation to the cell status of normality and malignancy, but also their dielectric properties. There are reports showing that the cytoplasmic conductivity increases with an increasingly malignant phenotype [15]. Electrical measurements using normal and four cancerous cell lines in culture showed that breast cancer cell lines exhibit higher values of dielectric constants than healthy cells, each type of cancer line having unique dielectric signature [16]. Measurements between 200 kHz and 5 MHz on breast normal and cancer cells in suspension indicate that conductivity is more than double in breast cancer cell MCF-7 than normal glandular mammary epithelial cell MCF-10A and relative permittivity is also higher in malignant cells [17]. Tumor tissues are characterized by higher conductivity comparing to normal tissues [18]. Measurements between 10 Hz to 1 MHz show that conductivity increases with necrosis percentage [19]. Using Time Domain Spectroscopy technique, resulted that melanoma samples have higher refractive index and absorption coefficient than normal skin with the same fibroblast density, in the frequency range 0.4–1.6 THz [20]. The open-ended coaxial probe method was applied on normal and cancerous tissues collected surgically and results show that the dielectric constant of colon cancerous tissue and its conductivity are higher [21]. From measurements on breast cancer tissues within 0.5–50 GHz resulted that, malignant tissues have higher values of dielectric constants due to their higher water content [22].

Based on several experimental studies presented in literature, the authors of [23] reveal some significant structural alteration when normal cells are compared to cancer cells: *"the deficiency of lipoproteins in plasma membrane and lack of fatty acids in phospholipids make membrane more diluted, deformed and alleviated … water become an excessive constituent"*. Under such conditions, important

changes occur in the bio-chemical and physical properties (electrical, mechanical) of the membrane and its behavior is modified when exposed to high intensity electric field. The membrane conductivity and dielectric constant are higher for the cancer compared to normal cells. The authors of the study mentioned above have analyzed (by numerical simulations) the electropermeabilization of human breast cells MCF-10A (normal) compared to MCF-7 (cancer) and concluded that, when exposed to similar electrical stress, cancer cells are more sensitive than their normal counterparts (electropermeabilization is triggered faster, pore density is higher, field strength threshold is lower), due to their higher dielectric properties.

Taking into account all these experimental data, the subsequent numerical simulations were performed under the following assumptions:

1. 2D *geometry*. The electric field problem was solved for the 2D cell model using the commercial software COMSOL Multiphysics, previously verified in similar cases [24].

2. *Three-layers model*. Each cell was modeled as a structure with three layers, based on the shapes determined from PIs for all four categories of cells (as shown in Fig. 1). The calculation domain was limited to a square of 70×70 μm^2 and included: i/ the cell with its three domains (nucleus, cytoplasm, and membrane with a thickness of 0.4% of the cytoplasm mean radius) and ii/ the extracellular fluid. ITV was computed as a result of applying an electric field of 1 kV/cm continuous wave inside the rectangular enclosure, by setting adequate electric potential boundary conditions on the upper and bottom boundaries of the calculation domain and electric insulation on the lateral boundaries.

3. *Electrical parameters*. For the cells category with lower malignancy level (B16F1), the dielectric properties – electrical conductivity σ and relative permittivity ε – were taken from literature as for nonmalignant cells and given their dependence on the electric field frequency [24–27]. For the other cell categories, higher values were tested, in intervals correlated with the determined phase shift values.

Taking advantage of the fact that the PIs offer the main compartments of the cell separately, we chose to work at the frequency of 1 GHz. Motivation is based on the observation [28] that at higher frequencies (> hundreds of kHz) membrane permeability increases and the electric field penetrates into the whole cell, to the nucleus and other organelles, unlike the case of lower frequencies (up to few kHz) where the plasma membrane represents an insulating shield, which completely hides the cell interior from the external applied electric field. Between 0.1 and 5 GHz, delta dispersion indicates an abrupt variation of the membrane dielectric constant. It was first observed in a study by Pethig [29] and was attributed to the polarization phenomena that involve the dipolar moments of proteins and other large molecules [30], and protein-bound water molecules [31]. Therefore, we can say that protein content influences the dielectric properties of cells. On the other

hand, phase shift values are linked with the dry mass of the cell and consequently are proportional to the protein content [32].

From microscope phase images, it turned out that malignant cells have lower values for dry mass density than normal cells [13, 14, 33], indicating a higher amount of solvent (water). It is already recognized [34] that formation of aqueous pores in the lipid bilayer is the principal mechanism at molecular level which induces the electroporation process. For these reasons, and tacking into account the before mentioned measurements on cells [15–17] and tissues [18–21], we tested the ITV changes due to the increase in the values of electrical constants up to 20% from the values assigned to the normal cell. This percentage was chosen to fit the variation of the dry mass density between normal and malignant cells deduced from the phase information [33]. For the B16F1-E cells we attributed the dielectric constant values for normal cells, as estimated in [24, 27]. For the other cell categories, the values were scaled following a linear dependence according to the phase shift values depicted in Table 1. The values used in our simulations are listed in Table 2, assigned as Case 1 to Case 4.

Table 2

Dielectric properties attributed to cell components on four cases

	Cell type	σ_{ext} (S/m)	σ_{cyto} (S/m)	σ_{mem} (S/m)	σ_{nucl} (S/m)	ε_{ext}	ε_{cyto}	ε_{mem}	ε_{nucl}
Case 1	B16F1-E	1.9200	1.9200	0.0120	0.3000	75.500	75.5000	4.000	52.0000
Case 2	B16F10-E	1.9200	1.9446	0.0127	0.3027	75.500	76.4668	4.230	52.4639
Case 3	B16F1-R	1.9200	2.1536	0.0131	0.3345	75.500	84.6843	4.480	57.9732
Case 4	B16F10-R	1.9200	2.2080	0.0138	0.3450	75.500	86.8250	4.600	59.8000

The main data used for numerical analysis at our four types of cases, are listed below going through the following steps:

1. First, a highly simplified model is defined, with circular shapes (Fig. 2) forming three concentric domains: nucleus, cytoplasm, membrane (with the radial dimensions $R_{nucl} = 8$ μm, $R_{cyto} = 20$ μm, cellular membrane thickness 5 nm). The uniform electric field is applied as shown in Fig. 2.

2. As a reference for evaluating the results, a model with circular shapes forming two domains: cytoplasm and membrane is also defined ($R_{cyto} = 20$ μm, cellular membrane thickness 5 nm).

3. Realistic cellular shapes from digital holographic microscopy are used for the construction of three-layer realistic models with the main components: nucleus, cytoplasm, membrane.

4. Realistic cellular shapes from digital holographic microscopy in the absence of the nucleus (*i.e.* two-layer realistic models).

For each model and case, the dielectric properties are taken from Table 2, as needed.

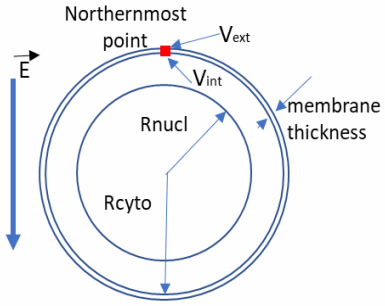

Fig. 2 – Schematic view of the three-layer model with circular shapes.

4. RESULTS

Figure 3 shows the evolution of the ITV values (defined as $V_{int} - V_{ext}$) in the northernmost point of the circular cell model (*i.e.* position for the extreme value of ITV on the cell membrane), when we varied the values of the electrical parameters for each domain, one by one (between Case 1 and Case 4: Fig. 3a only the nucleus parameters, Fig. 3b only the cytoplasm parameters, Fig. 3c only the membrane parameters), keeping the other domains with constant electrical properties.

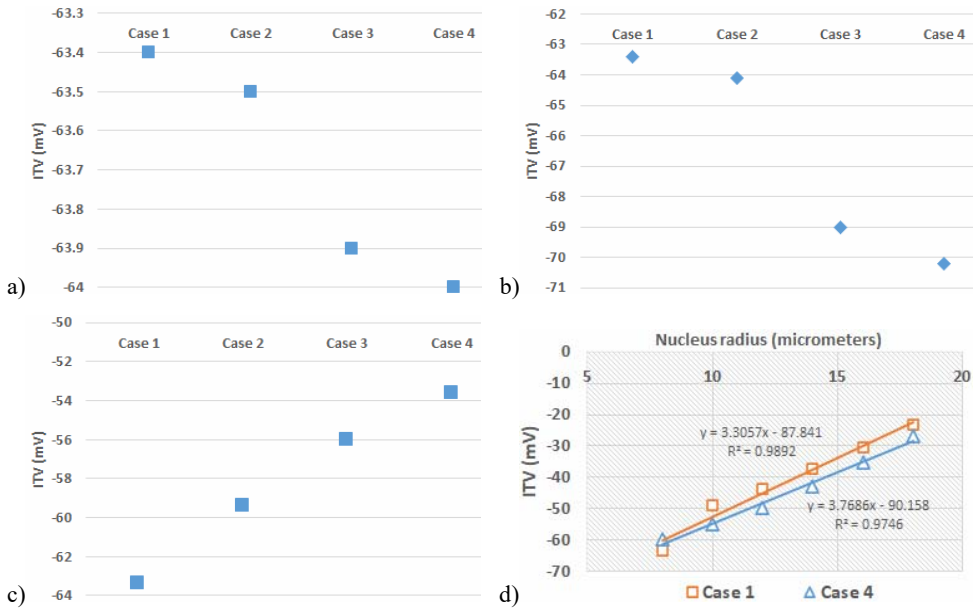

Fig. 3 – ITV when the properties are varied only for one domain at a time, *i.e.*: a) nucleus; b) cytoplasm; c) membrane, keeping the other domains with constant electrical parameters; d) ITV for the circular cell model, when the nucleus radius is varied.

Cells with high level of malignancy have a larger nucleus than normal cells. To mimic the variation in the ratio between the mean radius of the nucleus and that of the whole cell, we varied the radius of the nucleus between 8 and 18 µm, in two distinct data sets of dielectric properties (Table 2, Case 1 and Case 4); in this case, ITV values in the northernmost point are presented in Fig. 3d.

This study aims further to highlight the importance of considering the nucleus as a distinct component of the cell structure. The ITV maximum values are computed for all dielectric properties, in the cases of circular three-layer against two-layer models with dielectric properties given in Table 2. In Fig. 4 one could see that the presence of nucleus lowers by approx. 15% the ITV maximum absolute values.

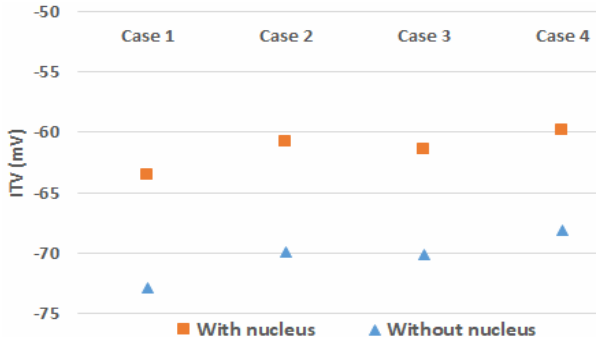

Fig. 4 – ITV of each circular cell model with dielectric properties from Table 2; comparison between the three-layer (the nucleus is included) and two-layer (the nucleus is absent) models.

Electric field spectra are built and analyzed for each cell model: four realistic cell models shown in Fig. 1, with and without considering the presence of the nucleus. The exposure is performed in continuous wave electric field of 1 kV/cm at 1 GHz and the dielectric cell properties are assumed as in Table 2.

Color maps with the distribution of the electric potential for each cell type are illustrated in Fig. 5, superposed with arrows of the electric field strength, tangent at field lines and perpendicular to the equipotential lines. It can be observed that the electric potential distribution is very little affected by the cell.

Membrane conductivity shows a wide variation between the low frequency range (kHz) and the high frequency range (GHz). Therefore, at low frequencies the membrane acts practically as an insulating shield, preventing the electric field from entering the cell, unlike in the case of high frequencies, where the electric field crosses almost unaffected, thus reaching the internal organelles, like the nucleus (Fig. 5). These results are consistent with the conclusions of the theoretical and experimental investigations reported in literature [28, 35, 36].

The distribution of the ITV values along the cell contour is presented in Fig. 6: top row – cells with nucleus, bottom row – cells without nucleus. The electric potential variations along the nucleus contour are shown in Fig. 6 middle row. On the O*x* axis are represented distances in micrometers, along arclength of the membrane or nucleus contour.

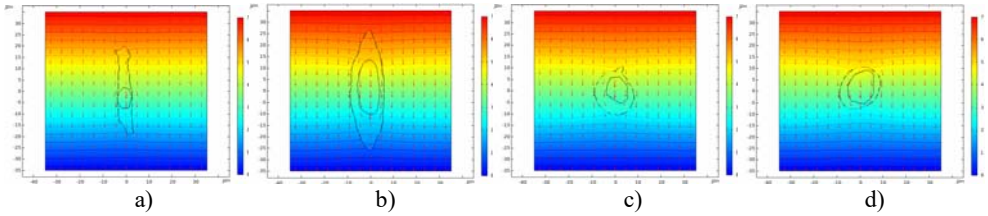

a) b) c) d)

Fig. 5 – Representation of the electric potential (colormap) and electric field strength (arrows) for all cell categories: a) B16F1-E; b) B16F10-E; c) B16F1-R; d) B16F10-R in three-layer models.

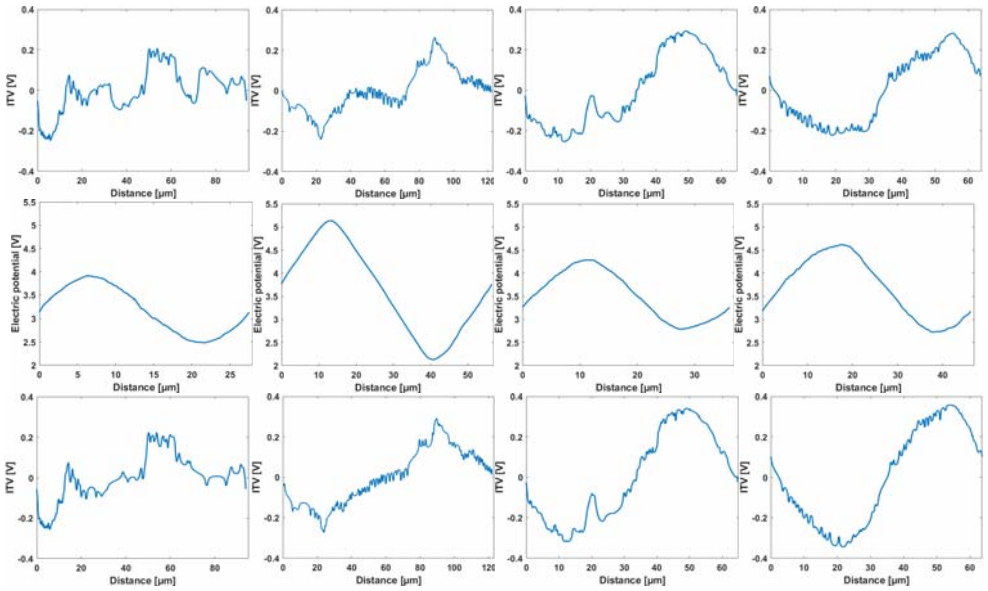

a) b) c) d)

Fig. 6 – ITV variation along the entire 2D cell contour with nucleus (top row) / without nucleus (bottom row), electric potential variation along nucleus contour (middle row):
a) B16F1-E; b) B16F10-E; c) B16F1-R; d) B16F10-R.

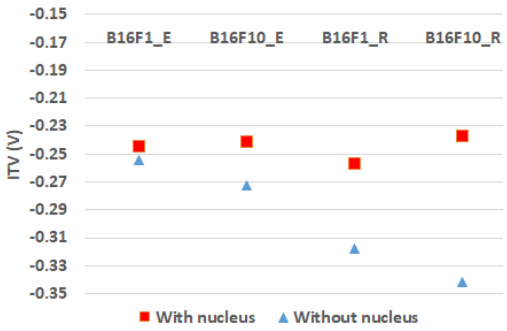

Fig. 7 – ITV for all four realistic cell's categories in the presence / absence of the nucleus.

We collected the ITV values at the northernmost point in Fig. 5; their variation is represented in Fig. 7 (red rectangles). The importance of the nucleus presence in the simulations was tested again, this time with the realistic shape models, by collecting the ITV values if the nucleus was removed from the computational domain (Fig. 7 blue triangles).

5. CONCLUSIONS

Experimental holograms of cells were used to build realistic models which were used for the numerical simulations of the electric field problem in EP. Segmentation of PIs was performed to maximize the accuracy of the calculated values on cells compartments. A three layers model was used assigning dielectric parameters to fit dry mass density variation between normal and malign cells. The distributions of the electric field and induced transmembrane voltage were obtained for four cell categories (two malignancy levels with elongated and round shapes) segmented in their main compartments.

The initial step was to consider highly simplified circular shapes for the cells, to test ITV evolution at different values of dielectric properties (conductivity and relative permittivity), varied in turn, each time for a single domain. It is observed that the greatest influence is that of the membrane.

The influence of the nucleus on the simulation results was tested by varying its radius in reasonable limits and by taking into account its presence or absence. ITV values were affected by up to 30%.

One of the aims of this study was to propose a new method for better assessment of cytoplasm and nucleus conductivity, which is critical to the development of electroporation protocols, considering information from microscopical measurements about the phase shift.

As further developments, the model may be adapted for various electric field waveforms and the simulation may characterize the membrane electropermeabilization process. Numerical simulation proves thus its flexibility and usefulness as a research tool, complementary to biophysical laboratory experiments.

Acknowledgements. A. M. P. and R. D. N. acknowledge to HOLOPROC project UPB Proof of Concept /2020. V. L. C. acknowledges to PED525/2020 Cytosin project. Holograms acquisition was done at OPTOELECTRONICA 2001 SA, using commercial DHM^{TM} from Lynceetec.

REFERENCES

1. M. L. Yarmush, A. Golberg, G. Serša, T. Kotnik, D. Miklavcic, *Electroporationbased technologies for medicine: Principles, applications, and challenges*, Ann. Rev. Biomed. Eng. **16**, 295–320 (2014).
2. M. Scuderi, M. Rebersek, D. Miklavcic, J. Dermol-Cerne, *The Use of High-frequency Short Bipolar Pulses in Cisplatin Electrochemotherapy in Vitro*, Radiol. Oncol. **53**, 194–204 (2019).
3. K. N. Aycock R. V. Davalos, *Irreversible Electroporation: Background, Theory, and Review of Recent Devices in Clinical Oncology*, Bioelectricity **1**, 214–234 (2019).

4. T. Kotnik, W. Frey, M. Sack, S. Haberl Meglic, M. Peterka, D. Miklavcic, *Electroporation-based application in biotechnology*, Tren. Bio. **33**, 480–488 (2015).
5. L. Lambricht, A. Lopes, S. Kos, G. Sersa, V. Préat, G. Vandermeulen, *Clinical potential of electroporation for gene therapy and DNA vaccine delivery*, Expert Opin. Drug Deliv **13**, 295–310 (2016).
6. T. Potocnik, D. Miklavcic, A. Macek Lebar, *Gene transfer by electroporation with high-frequency bipolar pulses in vitro*, Bioelectrochemistry **140**, 107803 (2021).
7. S. Mahnic-Kalamiza, E. Vorobiev, D. Miklavcic, *Electroporation in Food Processing and Biorefinery*, J. Membr. Biol. **247**, 1279–1304 (2014).
8. A. Golberg, M. Sack, J. Teissie, G. Pataro, U. Pliquett, G. Saulis, T. Stefan, D. Miklavcic, E. Vorobiev, W. Frey, *Energy-efficient biomass processing with pulsed electric fields for bioeconomy and sustainable development*, Biotech. Biof. **9**, 94 (2016).
9. H. P. Schwan, *Electrical properties of tissue and cell suspensions*, Adv. Biol. Med. Phys. **5**, 147–209 (1957).
10. B. Kemper, A. Bauwens, D. Bettenworth, M. Götte, B. Greve, L. Kastl, S. Ketelhut, P. Lenz, S. Mues, J. Schnekenburger, A. Vollmer, *Label-Free Quantitative In Vitro Live Cell Imaging with Digital Holographic Microscopy*, Wegener, J. (ed), in: *Label-Free Monitoring of Cells in vitro. Bioanalytical Reviews*, **2**, Springer, 2019, pp. 219–272.
11. M. Hellesvik, H. Øye, H. Aksnes, *Exploiting the potential of commercial digital holographic microscopy by combining it with 3D matrix cell culture assays*, Sci. Rep. **10**, 14680 (2020).
12. P. Jourdain, D. Boss, B. Rappaz, C. Moratal, M.-C. Hernandez, C. Depeursinge, P. J. Magistretti, P. Marquet, *Simultaneous Optical Recording in Multiple Cells by Digital Holographic Microscopy of Chloride Current Associated to Activation of the Ligand-Gated Chloride Channel GABAA Receptor*, Plos One **7**, e51041 (2012).
13. M. Mihailescu, I. A. Paun, E. Vasile, R. C. Popescu, A. V. Baluta, D. G. Rotaru, *Digital off-axis holographic microscopy: from cells visualization to phase shift values, ending with physiological parameters evolution*, Rom. J. Phys. **61**, 1009–1027 (2016).
14. V. L. Calin, M. Mihailescu, E. I. Scarlat, A. V. Baluta, D. Calin, E. Kovacs, T. Savopol, M. G. Moisescu, *Evaluation of the metastatic potential of malignant cells by image processing of digital holographic microscopy data*, FEBS Open Bio. **7**, 1527–1538 (2017).
15. C. I. Trainito, D. C. Sweeney, J. Čemazar, E. M. Schmelz, O. Francais, B. Le Pioufle, R. V. Davalos, *Characterization of sequentially-staged cancer cells using electrorotation*, PLoS One **14**, e0222289 (2019).
16. M. Hussein, F. Awwad, D. Jithin, H. El Hasasna, K. Athamneh, R. Iratni, *Breast cancer cells exhibits specifc dielectric signature in vitro using the open-ended coaxial probe technique from 200MHz to 13.6GHz*, Sci Rep. **9**, 4681 (2019).
17. Y. Wang, Y. Li, J Huang, Y. Zhang, R. Ma, S. Zhang, T. Yin, S. Liu, Y. Song, Z. Liu, *Correlation between electrical characteristics and biomarkers in breast cancer cells*, Sci. Rep. **11**, 14294 (2021).
18. A. Kiełbik, W. Szlasa, J. Saczko, J Kulbacka, *Electroporation-Based Treatments in Urology*, Cancers **12,** 2208 (2020).
19. D. Haemmerich, S.T. Staelin, J.Z Tsai, S. Tungjitkusolmun, D.M. Mahvi, J.G. Webster, *In vivo electrical conductivity of hepatic tumors*, Physiol. Meas. **24**, 251–260 (2003).
20. R. Zhang, K.Yang, B. Yang, N. A. AbuAli, M. Hayajneh, M. Philpott, A. Alomainy, *Dielectric and double debye parameters of artificial normal skin and melanoma*, J. of Infrared, Millim, and Terahertz Waves **40**, 657–672 (2019).
21. A. Fornes-Leal, C. Garcia-Pardo, M. Frasson, V. Pons Beltrán, N. Cardona, *Dielectric characterization of healthy and malignant colon tissues in the 0.5–18 GHz frequency band*, Phys Med. Biol. **61**, 7334–7346 (2016).
22. A. Martellosio, M. Pasian, M. Bozzi, L. Perregrini, A. Mazzanti, F. Svelto, P.E. Summers, G. Renne, M. Bellomi, *0.5–50 GHz dielectric characterisation of breast cancer tissues*, IET Electron. Lett. **51**, 974–975 (2015).

23. M. A. Aslam, K. Riaz, M. Q. Mahmood, M. Zubair, *Hybrid analytical-numerical approach for investigation of differential effects in normal and cancer cells under electroporation*, The Royal Society of Chemistry Adv. **9**, 41518–41530 (2019).
24. A.-M. Sandu, M. A. Ungureanu, M. Morega, V. L. Călin, M. G. Moisescu, I. A. Paun, M. Mihailescu, *Realistic models of cultured cells for electroporation simulations starting from phase images*, Proc. SPIE 11718, X, 117180W (2020).
25. T. Kotnik, D. Miklavcic, *Second-Order Model of Membrane Electric Field Induced by Alternating External Electric Fields*, IEEE Trans. on BME **47**, 1074 (2000).
26. L. Towhidi, D. Khodadadi, N. Maimari, R. M. Pedrigi, H. Ip, Z. Kis, B. R. Kwak, T. W. Petrova, M. Delorenzi, R. Krams, *Comparison between direct and reverse electroporation of cells in situ: a simulation study*, Physiol Rep. **4**, e12673 (2016).
27. C. Merla, M. Liberti, F. Apollonio., G. D'Inzeo, *Quantitative Assessment of Dielectric Parameters for Membrane Lipid Bi-Layers from RF Permittivity Measurements*, Bioelectromagnetics **30**, 286–298 (2009).
28. A. De Angelis, A. Denzi, C. Merla , F. M. Andre, T. Garcia-Sanchez, L. M. Mir, F. Apollonio, M. Liberti, *A Microdosimetric Realistic Model to Study Frequency-Dependent Electroporation in a Cell with Endoplasmic Reticulum*, 49th European Microwave Conf. (EuMC), 2019, 19186827.
29. R. Pethig, *Dielectrophoresis: Theory, Methodology and Biological Applications*, John Wiley & Sons NJ, USA, 2017.
30. K. Asami, *Characterization of biological cells by dielectric spectroscopy*, Journal of Non-crystalline Solids **305**, 268–277 (2002).
31. M. Gotz, L. Karsch J. Pawelke, *A new model for volume recombination in plane-parallel chambers in pulsed fields of high dose-per-pulse*, Phys in Med. & Biol. **62**, 8634–8654 (2017).
32. R. Barer, *Refractometry and interferometry of living cells*, J. Opt. Soc. Am. **47**, 545–556 (1957).
33. D. Roitshtain, L. Wolbromsky, E. Bal, H. Greenspan, L. Satterwhite, N. T. Shaked, *Quantitative Phase Microscopy Spatial Signatures of Cancer Cells*, Cytometry Part A **91**, 482–493 (2017).
34. T. Kotnik, L. Rems, M. Tarek, D Miklavcic, *Membrane Electroporation and Electropermeabilization: Mechanisms and Models*, Annual Rev of Biophys. **48**, 63–91 (2019).
35. G. Pucihar, D. Miklavčič, T. Kotnik, *A time-dependent numerical model of transmembrane voltage inducement and electroporation of irregularly shaped cells*, IEEE Trans. Biomed. Eng. **56**, 1491–1501 (2009).
36. M. Liberti, F. Apollonio, C. Merla, G. D'Inzeo, *Microdosimetry in the microwave range: A quantitative assessment at single cell level*, IEEE Ant. Wirel. Propag. Lett. **8**, 865–868 (2009).